Synthesis of high-surface-area C$_3$N$_4$ deposited on halloysite-derived silica nanotubes: Enhanced visible light degradation of norfloxacin

L. Santamaría [a,b,*], S.A. Korili [b], A. Gil [b], J.M. López-de-Luzuriaga [a], M. Monge [a,**]

[a] Departamento de Química, Centro de Investigación en Síntesis Química (CISQ), Complejo Científico Tecnológico, Universidad de La Rioja, Madre de Dios 53, Logroño 26006, Spain
[b] INAMAT2, Departamento de Ciencias, Edificio de los Acebos, Universidad Pública de Navarra, Campus de Arrosadía, Pamplona E-31006, Spain

ARTICLE INFO

ABSTRACT

Silica nanotubes, obtained from halloysite clay nanotubes that were calcined and acid-activated, were used as support for graphitic carbon nitride (g-C$_3$N$_4$) via a simple deposition method. They were chosen in order to avoid any agglomeration issues, as there was an increase of the specific surface area with respect to pristine halloysite. The composite was tested for the degradation of a persistent emerging pollutant in water, namely, antibiotic norfloxacin. Experiments were performed in darkness (until adsorption-desorption equilibrium was attained) and, subsequently under visible light. Comparison of the performance between the photocatalysts shows that the composite was 49% faster than g-C$_3$N$_4$. The introduction of persulfate in the lumen of the nanotubes via vacuum negative-pressure suction and injection was also tested for the generation of ·OH radicals that fasten the degradation rate, obtaining a further 47% increase in the degradation rate of norfloxacin thanks to the release of this anion during the photodegradation process. The degradation mechanism of SiO$_2$/g-C$_3$N$_4$ sample was studied with trapping experiments by the use of scavengers that were introduced to quench the photodegradation: triethanolamine for photoexcited holes ($h+$), tert-butanol for hydroxyl radicals (·OH) and a N$_2$ atmosphere for superoxide radicals (·O$_2^-$).

1. Introduction

According to the European Environmental Agency, the state of Europe's water can be greatly improved, with only 38% of surface waters in good chemical status [17]. More than 700 emerging pollutants are present alone in the European aquatic environment [23]. These are chemicals or microorganisms not commonly monitored and yet with the potential to enter the environment and cause ecological/human health effects. In order to tackle the protection of surface and groundwater against new pollutants, the European Commission proposes an updating of the list of water pollutants to be more strictly controlled [16]. Among them, antibiotics are considered one of the main threats to the environment due to its worldwide growing consumption, an estimated 46% rise since 2000 [6], or the fact that these substances are not completely metabolized by animals or humans (in the case of Norfloxacin, a 30% is readily excreted unchanged [50]), reaching the environment since wastewater treatment plants are not capable of retaining them. These

compounds, together with analgesic and anti-inflammatory drugs, are found to exert the highest toxic pressure on aquatic ecosystems [21]. One of the main threats that antibiotics generate is the promotion of antibiotic resistance within the local bacterial populations in the environment and wastewater plants [45], which are already responsible for a growing number of infection accounting for more than 30000 deaths in Europe per year [7]. Norfloxacin, a synthetic fluoroquinolone antibiotic is commonly detected in wastewater effluents [36]. Prolonged exposure to a low dose of this antibiotic changes immune function of fish and can damage their intestine and cause a stress response [69]. There is, thus, a need for finding a cost-effective method to remove organic pollutants that can cause such a threat to both the environment and human health. Among the different methods readily available there are some that have proven to be effective against stubborn organic pollutants, such as adsorption or coagulation. These do not eliminate the pollutant but concentrate it and the use of other methods such as filtration or chemical and membrane technologies can generate toxic secondary pollutants,

* Corresponding author at: Departamento de Química, Centro de Investigación en Síntesis Química (CISQ), Complejo Científico Tecnológico, Universidad de La Rioja, Madre de Dios 53, Logroño 26006, Spain.
** Corresponding author.
E-mail addresses: leticia.santamaria@unirioja.es (L. Santamaría), miguel.monge@unirioja.es (M. Monge).

apart from having high operational costs [22]. Advanced oxidation processes such as photocatalysis is a wastewater treatment method that has gained great popularity for the production of green energy [25,64] or the elimination of emerging pollutants [63]: this low-cost technology is very promising as, with the aid of semiconductors, harmful antibiotics could be directly decomposed into much harmless products under solar-light illumination. Electrons and holes can activate both O_2 and H_2O which, in turn, generate reactive oxygen species such as hydroxyl radical ($\cdot OH$) or superoxide radical ($\cdot O_2^-$) that exhibit strong oxidation of organic matters transforming them to CO_2 and H_2O. However, the real application of semi-conductor photocatalysts is greatly restricted due to poor photocatalytic performance when dealing with persistent organic pollutants, as some of them (e.g. bisphenol A, norfloxacin, 4-Nitro-m-cresol…) are stable and have high oxidation potentials [65], hence the importance of fabricating a high-performance catalyst.

From the different semiconductors that can be used as photocatalysts, graphitic carbon nitride (g-C_3N_4) is one of the most promising ones as it has several features that make it appealing: it is low cost and chemically stable; has a narrow band gap (2.7 eV) that can exploit light in the visible spectrum, while being also easily synthesizable and environmentally friendly. However, several of these photocatalyst features must be improved in order to make it more effective for this task since its visible light absorption window is very narrow, its surface area is in the lower range and it also has a high photoinduced electron-hole recombination rate [42,58]. Moreover, its practical application is limited to low quantum efficiency due to severe agglomeration and large grain size resulting from uneven heat transfer, low mass transfer and deamination polycondensation during the calcination of the precursor [70]. Different strategies can be followed to tackle these issues such as changing its morphology into nanostructures such as nanoparticles or nanotubes [56] or doping the semiconductor with metallic or nonmetallic elements such as O, S and P with can be used to tune the electronic structure to a better visible-light-absorber catalyst [14]. The construction of heterojunctions can boost the efficient spatial charge separation [42]. Such heterojunctions can be obtained in the intermediate phases (mainly melem and melon) during the condensation of melamine to ideal graphitic carbon nitride and, thus, choosing an appropriate temperature in the catalyst synthesis can significantly improve its performance as a higher degree of polycondensation does not necessarily translate into better results [57]. On the other hand photocatalytic activation can be performed with the use of a synergistic mechanism between g-C_3N_4 and photoactivated sulfate radicals which ensures the generation of $\cdot OH$ radicals that fasten the degradation rate [28]. Another strategy to step up efficiency, and also followed in this paper, consists of providing the carbon nitride with a support in the synthesis process. The agglomeration of the catalyst is then hindered and, consequently, due to an increase of the surface area of the semiconductor, a boost of performance can be registered. Different clays have been explored as supports as they are easy to obtain on a big scale, such as zeolites [46], hydrotalcites [49] or halloysite. Halloysite was selected as support for the g-C_3N_4 due mainly to its special nanostructure. Halloysite is a 1:1 clay mineral is formed from aluminosilicate sheets: tetrahedral (Si-O) combine with octahedral (Al-OH) in a kaolinite manner, although in this case forming a nanotubular morphology. The chemical formula of raw halloysite is given as $Al(OH)_4Si_4O_5 \cdot nH_2O$. When n=2, 2<n<0 or n=0, the minerals are named hydrated halloysite, mixture of hydrated and dehydrated halloysites, and metahalloysite, respectively [15]. This widespread clay could be considered as a cheap alternative to carbon nanotubes, as it has similar shape, size, chemical stability and has the advantage of being much safer for water [11,18]. Halloysite has been lately used with other semiconductors such as TiO_2 [2] or MoS_2 [2] to improve photocatalytic reactions for water treatment. Also its nanotubes have been combined with other nanoparticles such as gold for the selective reduction activity for nitrobenzene compounds [13] or CdS nanospheres for water splitting purposes [35]. Halloysite was chosen in the present study as a guide to wrap the g-C_3N_4 around as it shows several appealing features: it is

cheap; naturally found; of nanotube morphology; with tunable surface; high adsorptivity potential; and higher BET surface than g-C_3N_4 [32,44]. This clay has been previously used as a template for the formation of nanocomposites with g-C_3N_4, although the whole halloysite structure has been used as support [9,29,40] or as a template in which the halloysite disappears in the synthesis process [56]. The novelty of this work comes from an acid activation of the clay that caused the removal of the Al-OH layer leaving a SiO_2 nanotube structure in which C_3N_4 was deposited. This shape was also used for the introduction of persulfate within the lumen improving with these characteristics the catalytic performance of g-C_3N_4.

2. Experimental procedure

2.1. Materials

Halloysite nanotubes were kindly supplied by Imerys (Matauri Bay, New Zealand). The reagents employed for the synthesis of the nanocomposites were: Melamine (99%, Acros Organics), potassium persulfate (> 99%, Sigma Aldrich) and hydrochloric acid (35%, Panreac). HPLC-grade acetonitrile was provided by Scharlab (Barcelona, Spain) and formic acid (98%) for HPLC was from Fluka Analytical.

2.2. Nanocomposites synthesis

SiO_2 nanotubes were prepared by a halloysite modification using an altered procedure from Wang et al. [56]. The initial chemical structure of the nanotubes was modified as displayed in Fig. 1. The procedure was: 10 g of halloysite was first calcined at 850 ºC for 2 h, then an activation of the nanotubes took place by introducing the powder in 100 mL of HCl 5 M at 80 ºC for 2 h, thus the inner alumina layer was withdrawn. The suspension was filtered off and washed with water until the washing water reached a pH of 7. Then, the solid was dried for 16 h. The next step consists of placing 1 g of this activated halloysite in a small crucible surrounded by 5 g of melamine. This was placed in a bigger crucible (see Fig. 2) and covered with aluminum foil to prevent the sublimation of the precursor. Treatment at 500 ºC for 4 h (heating rate of 20 °C/min) and then at 520 ºC for another 2 h in order to obtain exfoliated g-C_3N_4 nanosheets [61] produced the polycondensation of the melamine to obtain g-C_3N_4 powder. In this process, the original halloysite acquired a pale-yellow color with the g-C_3N_4 coating (named SiO_2-C_3N_4, see Fig. 2) as did the powder placed in the bigger crucible which was collected as a reference (named g-C_3N_4).

2.2.1. Persulfate impregnation procedure

Potassium persulfate was loaded into the lumens of the SiO_2-C_3N_4 nanotubes via vacuum negative-pressure suction and injection [26]. The experimental procedure consisted in placing 3 g of K_2SO_8 in a double-necked round-bottom flask containing 150 mL of H_2O (Milli-Q) where it was magnetically stirred for 30 min. 0.5 g of SiO_2-C_3N_4 were added and an ultrasonic probe was employed in order to disperse the nanotubes for another 30 min. Taking away the flask from the stirrer, it was then attached to a vacuum line for 30 min. During the vacuum procedure, a large number of small air bubbles could be seen coming out to the surface, a sign of the release of the air inside the lumens. Vacuum was then interrupted and the solution was sonicated while being stirred for 30 min at atmospheric pressure to help the persulfate ions to be incorporated into the lumen of the nanotubes. Vacuum-sonication steps were repeated 3 more times to maximize persulfate injection rate. Persulfate-loaded SiO_2-C_3N_4 nanotubes were then separated from the solution by centrifugation for 15 min at 5000 rpm washing it with miliQ-water. This process was repeated three times in order to desorb all the persulfate that could be adsorbed to the nanotubes surface. The obtained sludge was then dried at 50 ºC for 48 h.
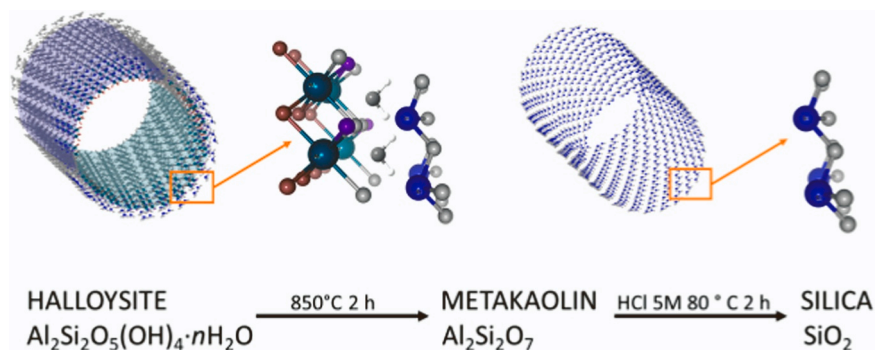
Fig. 1. Structural changes of the halloysite nanotubes subjected to thermal and acid treatment.

Fig. 2. Images of the vapor deposition procedure.

2.3. Characterization of the adsorbents

The assessment of the porosity and the crystallites surface of the samples was carried out by N_2 adsorption–desorption at −196 ℃ in a Micromeritics ASAP 2020 Plus adsorption analyzer. The samples (0.4 g) were degassed at 200 ℃ for 24 h under vacuum before measurement. The specific surface area was determined from adsorption data by applying the Brunauer–Emmett–Teller (BET) equation in the range between 0.05 and 0.20 of relative pressure. The external surface area (*Sext*) and the micropore volumes (*Vμp*) were also estimated using the *t-plot* method. Pore size distribution was derived from the adsorption branch of the isotherm by BJH (Barret–Joyner–Halenda) using Halsey–Faas correction. Powder X-ray diffraction (PXRD) was used to identify the crystalline phase of the samples. They were analyzed in a Bruker D8 Advance Eco X-ray diffractometer with Ni-filtered Cu Kα radiation (λ = 0.1548 nm) at a 2-theta range from 5 to 80° and a scanning rate of 2° (2θ)/min. The morphological analysis of the samples was carried out by Transmission Electron Microscopy (TEM). Samples were drop-casted from ethanol dispersions (2–3 drops) to carbon-coated Cu grids. The corresponding micrographs were acquired at a working voltage of 200 kV with a Tecnai T20 (ThermoFisher Scientific). Thermogravimetric/differential thermal analyzer (TG-DTA) measurement was conducted on a Mettler Toledo TGA/DSC 3+ apparatus under an air atmosphere (50 mL/min) and using a 10 ℃/min heating rate from room temperature up to 900 °C. Fourier-transform infrared spectroscopy (FTIR) was performed in a FT-IR Pelkin-Elmer Two spectrophotometer covering a range from 500 to 4000 cm^{-1}. Diffuse reflectance UV–vis spectra of the samples were recorded on a UV-3600 spectrophotometer (Shimadzu, Kioto, Japan) equipped with a Harrick Praying Mantis accessory and recalculated following the Kubelka-Munk function, leading to the solid-state absorption spectra. Excitation and emission spectra of the samples were recorded on a Shimadzu RF-6000 Spectrofluorophotometer. X-ray photoelectron spectroscopy (XPS) analyses were carried out on a Versaprobe III Physical Electronics (ULVAC) spectrometer equipped with a monochromatized Al Kαα X-ray source (1486.7 eV). The pass energy was set at 224 eV for the general spectra and at 27 eV for the elementary spectra. When required, spectra were decomposed with the CasaXPS 2.3.26 program (Casa Software Ltd., UK).

2.4. Norfloxacin photodegradation experiments

The photodegradation tests were performed using a Photolab Equipment (LED365–1/450–1/850–1cb, Apria Systems, Spain). 20 mg of the catalyst was placed in a petri dish containing 20 mL of Norfloxacin aqueous solution (10 ppm). Before irradiation, samples were stirred for 120 min in the dark in order to achieve an adsorption-desorption equilibrium. The visible lamp (radiation of 124 W/m^2) was then switched on and the photocatalyst performance was tested for other 120 min. During the whole procedure, aliquots of 1 mL were withdrawn every 15 min to monitor the norfloxacin concentration. The drug concentration in the filtered solutions (0.22 μmol, Durapore) was determined with an Agilent modular 1100/1200 liquid chromatography system (Agilent Technologies, USA) equipped with a G1329A autosampler and a G1315 diode array detector and a Phenomenex Luna LC C18 100 Å column. The mobile phase started 90:10 0.1% formic acid aqueous solution: acetonitrile with a 1.0 mL/min flow rate and an injection volume of 20 μL. Norfloxacin signal was measured at 275 nm. The catalytic photoreactions were carried out at natural pH and photolysis tests, in the absence of a catalyst, were also performed.

Trapping experiments were performed on the composite catalyst in order to detect the active species present in the degradation procedure. After the dark reaction, a certain number of scavengers, including triethanolamine and tert-butanol, to get a final 10^{-3} M concentration were added in order to quench hydroxyl radicals (·OH) and photogenerated holes (h^+), respectively. The existence of superoxide radicals (·O_2) was tested through the use of N_2 atmosphere in order to vent the oxygen present in the system [38,55,62].

3. Results and discussion

3.1. Catalysts characterization

As one of the benefits of the composite formation is the increase of the BET surface area, the textural properties of the samples at various stages were examined and the results are displayed in Fig. 3 and Table 1. All the isotherms correspond to a type IV in the IUPAC classification, which are given by mesoporous adsorbents. The presence of small hysteresis loops, caused by pores wider than 4 nm, is typical of this capillary condensation [54]. The S_{BET} of the dehydrated sample (metahalloysite) is 27 m^2/g, slightly lower than expected [39], which could be due to the presence of allophane in the structure [33] and, when dehydroxylated at 520 °C, only a slightly increment in the surface area was found (29 m^2/g). The acid activation of the nanotubes scraped the nanotubes of the octahedral inner layer (Al_2O_3) (see Fig. 1 and XPS results) and it is responsible for the strong increment in the S_{BET} up to 362 m^2/g, more porosity (especially on the micro and small mesoporous range, see Fig. 3b) and also the apparition of a number of acid centers [67]. The vapor deposition method was tested on both the metakaolin sample (without acid treatment) and the SiO_2 nanotubes, which led the g-C_3N_4
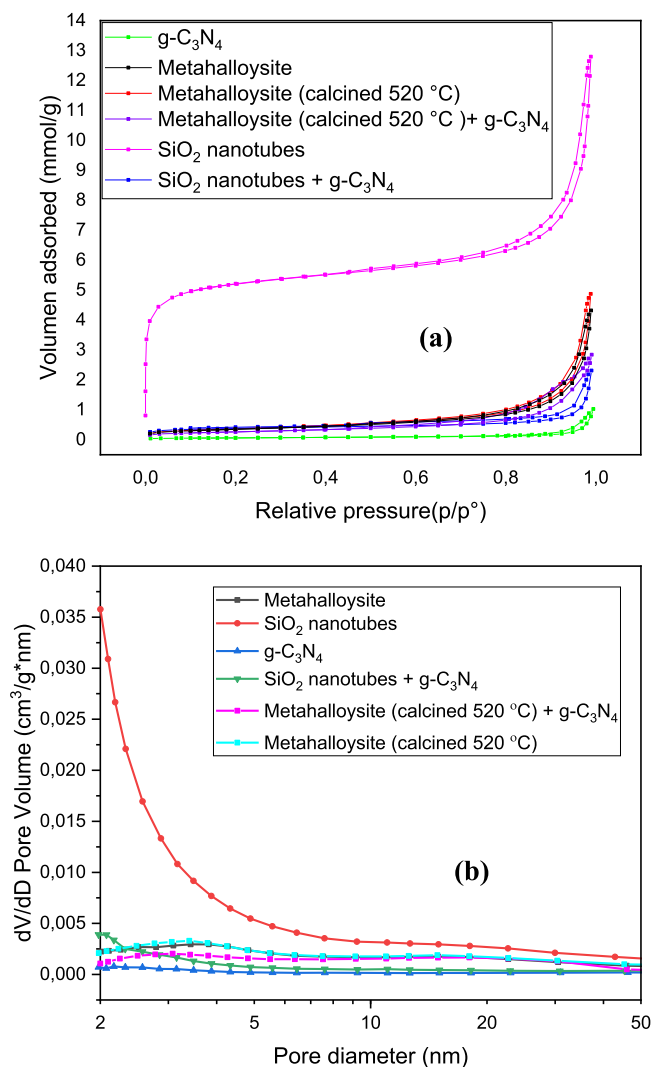
Fig. 3. The N$_2$ adsorption-desorption isotherms (a) and pore size distribution (b) of the samples.

Table 1
Textural properties of the halloysite/melamine-derived photocatalysts.

Sample	S_{BET} (m^2/g)	S_{ext} (m^2/g)	$V_{\mu p}$ (cm^3/g)
g-C$_3$N$_4$	5	4	0.0003
Metahalloysite (200 °C)	27	25	0.0014
Metakaolin (520 °C)	29	26	0.0012
SiO$_2$ nanotubes	362	123	0.1262
Metakaolin (520°C) + g-C$_3$N$_4$	20	18	0.0013
SiO$_2$ nanotubes + g-C$_3$N$_4$	26	15	0.0064

S_{BET} to a 4 and 5-time increment, respectively. The presence of the nanotubes in the catalyst could provide more active sites for adsorption (see Fig. 11) and surface reactions, and both may improve the photocatalytic degradation performance of the carbon nitride [41,48,60]. The differences in both samples could be also observed in the micropores volume (5 times more in the case of SiO$_2$ nanotubes) and, thus, in the amount deposited: while the SiO$_2$ nanotubes went from 1 g to 1.52 g after the vapor deposition, the metakaolin only incremented its weight in 0.20 g. SiO$_2$ nanotubes were thereby the samples chosen to continue with the experimental procedure.

The PXRD diffractogram of the clay without previous treatment (Fig. 4a) shows the peaks of halloysite (JCPDS 29–1487) located at
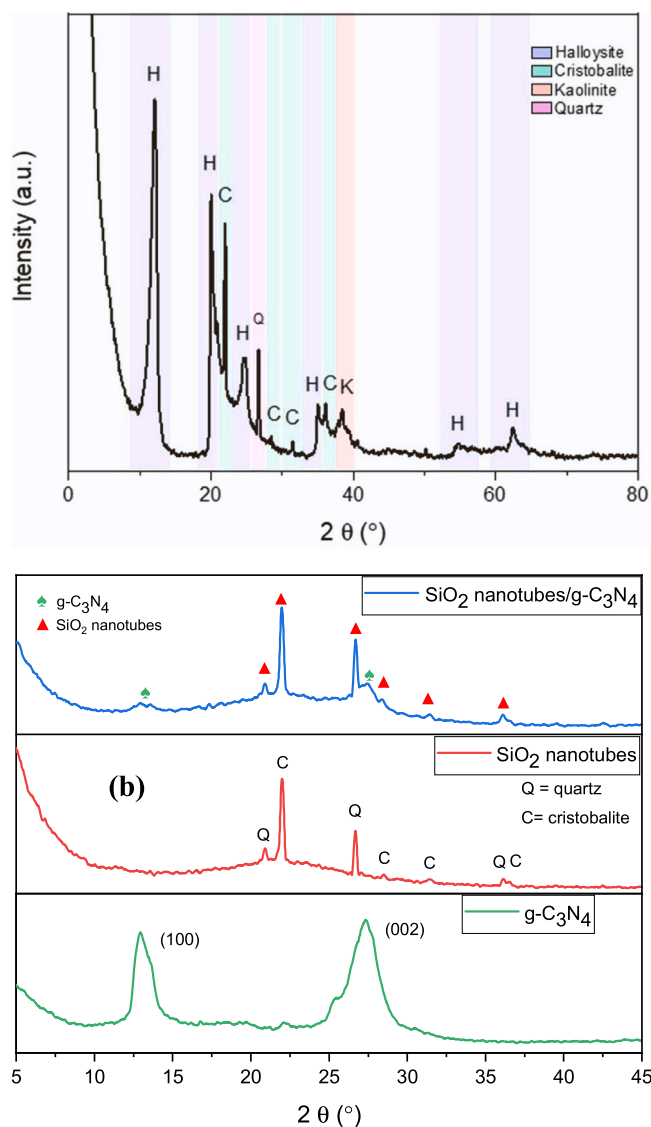

Fig. 4. Powder X-ray diffraction patterns of the as-provided halloysite (a) and of the g-C$_3$N$_4$, SiO$_2$ nanotubes and their combination (b).

12.16° (001), 19.99° (100), 24.74° (002), 35.06° (110), 54.86° (210) and 62.58° (300). Apart from the halloysite reflections, the presence of various secondary phases such as cristobalite at 22.00° (JCPDS 00–001–0438), quartz at 26.66° (JCPDS 01–083–2465) and kaolinite at 38.44° (JCPDS 01–083–0971), are usually found together with halloysite [10]. The halloysite sample is dehydrated as the reflection of 001 corresponds to a basal spacing of 7.31 Å, and it is similar to that of kaolinite. A intensity ratio smaller than 2 between the reflections of 001 and that at 19.99° (4.4 Å) may confirm the presence of halloysite-7Å [32], also known as metahalloysite. After the acid treatment all the peaks assigned to halloysite-kaolinite disappeared suggesting the total removal of the octahedral Al$_2$O$_3$ layer and leaving only the crystal structures corresponding to SiO$_2$, as both cristobalite and quartz (see Fig. 4b). On the other hand, the X-ray diffraction pattern of the bulk g-C$_3$N$_4$ sample, synthesized by thermal polycondensation of melamine, shows its two characteristic peaks: the first, at 2θ of 27.42°, the main peak, is labelled as the (002) plane and represents the distance between its layers, this being 0.326 nm. The intralayer d-spacing of 0.688 nm, is located at the second one, 2θ =12.92°, and it is attributed to the (100) plane [20]. The intensity of this peak is larger than that of pure g-C$_3$N$_4$ suggesting the presence of the intermediate melem phase (2,5,8-tri-amino-tri-s-triazine) or its derivatives, dimelem and melon [53], and it is

related to the temperature chosen for the polycondensation of the precursor. The incomplete polycondensation of melamine leaves small traces of intermediate derivatives. These intermediate phases can form heterojunctions and reduce the recombination of photogenerated charge carriers thus improving the photocatalytic performance of the material [43]. The diffractogram of the SiO_2 nanotubes with the deposited g-C_3N_4 confirms the formation of the composite with a combination of the peaks found in the separate SiO_2 nanotubes and bulk g-C_3N_4 patterns with no major changes in the (002) and (100) planes located at 27.37° (0.327 nm) and 13.06° (0.681 nm) respectively which can indicate a slight increase in the interlayer space and a small decrease in the intraplanar hole-to-hole distance [19].

TEM micrographs of the samples are shown in Fig. 5. The first image (Fig. 5a) shows the halloysite nanotubes after subjection to the acid treatment. Although being stripped of the octahedral alumina internal layer, the nanotube structure remains unaltered. The SiO_2 nanotubes have a length of about 600 nm, can be considered as long in comparison with other halloysite samples and have the characteristic form of the Matauri Bay quarry [32]. After the vapor deposition, (Fig. 5b), the g-C_3N_4 nanosheets with flat irregular shape can be seen effectively enveloping the nanotube. The nanotubes can succeed in acting as an anchor in which the catalyst can wrap around, thus reducing the agglomeration issue. TEM image of exfoliated g-C_3N_4 is displayed in Figure S1.

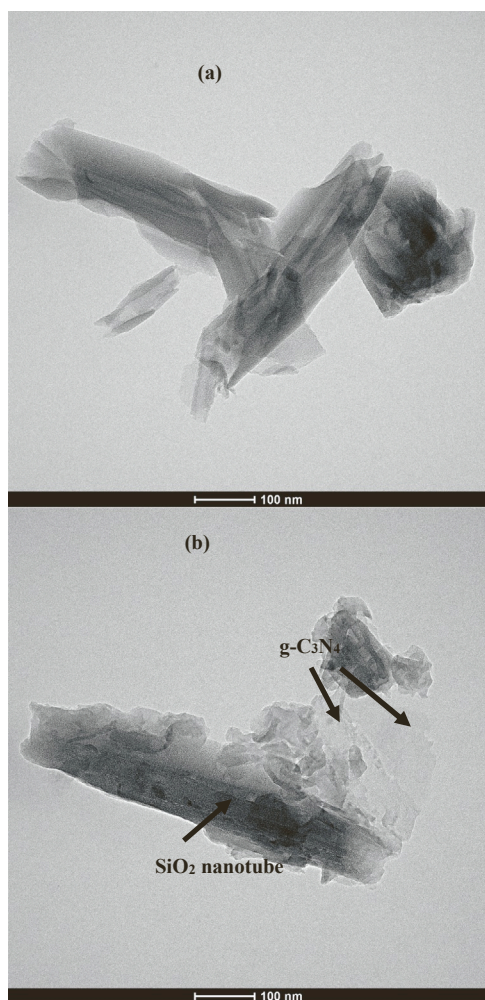Thermogravimetric analysis (TG-DTA) of the samples (Fig. 6) show

Fig. 6. TG and DTG curves of the exfoliated g-C_3N_4, SiO_2 nanotubes and their combination.

that the acid activated halloysite nanotubes have only one mass-loss step between the range of 50–150 °C ascribed to the loss of water inside the tubes or to gases/water adsorbed to the outside layer. This inside water or external gases/water would be lost in the early stages of the commented deposition procedure. The bulk g-C_3N_4 sample has an almost imperceptible mass-loss step (1.5%) before the 150 °C mark. From 500 °C and, mainly, in the 650–760 °C range, the total decomposition of the sample takes place. The decomposition of the SiO_2-C_3N_4 composite has a 3% water-loss before reaching 150 °C and a second step with a maximum at 700 °C due to the elimination of its deposited g-C_3N_4. The composition of the SiO_2-C_3N_4 sample is almost half in g-C_3N_4 (46%). This sample has a ~50 °C discrepancy in the loss of the carbon nitride when comparing to the bulk sample. The fact that pure g-C_3N_4 degrades at lower temperature could be due to a greater availability of the material, being more stable because of a better dispersion in the composite sample.

FTIR characterization of the samples can be seen in Fig. 7 and further confirms the presence of carbon nitride over the SiO_2 nanotubes. Typical peaks attributed to g-C_3N_4 can be found in both samples. Thus, the broad peak located between 2900 and 3500 cm^{-1} range is formed by adsorbed water molecules and the stretching vibration of -NH_2 and =N-H amines [5]. At 800 cm^{-1} appears the breathing mode of triazine units and between 1200 and 1600 cm^{-1} those due to the aromatic CN heterocycles [34]. The fact that some of these peaks are not completely developed, like the one at 1209 cm^{-1}, which corresponds to trigonal C-N(-C)-C,

Fig. 5. TEM micrographs of the samples: acid activated halloysite nanotubes (a), acid activated nanotubes after g-C_3N_4 vapor deposition (b) and exfoliated g-C_3N_4 (c).
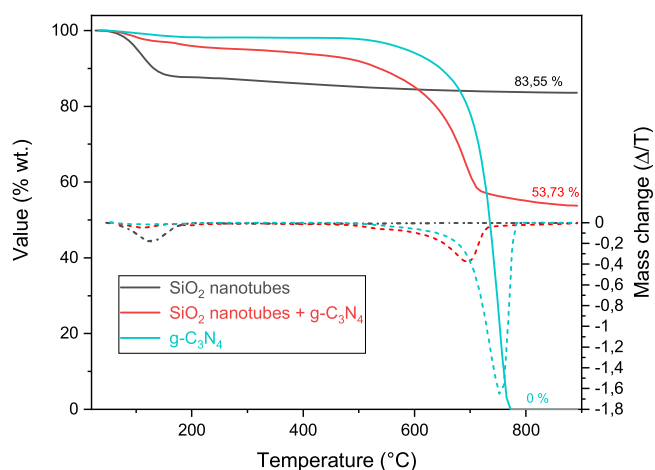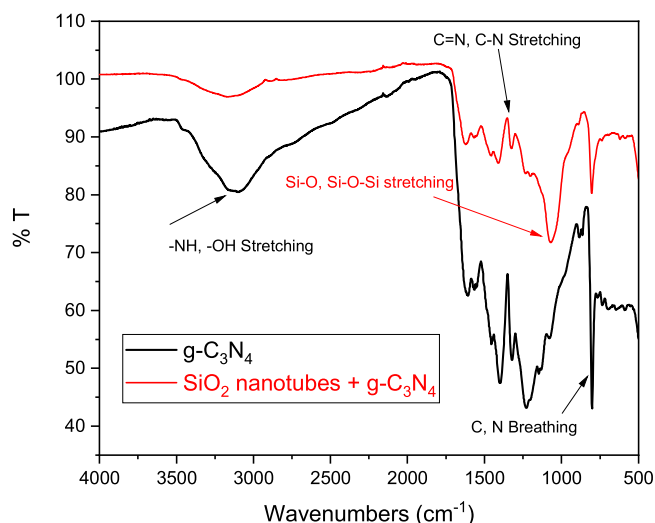

Fig. 7. FT-IR spectra of the exfoliated g-C_3N_4 and the SiO_2-C_3N_4 samples.

indicates that a more condensed polymer can be formed at higher temperature [57]. In the composite sample, a broad peak appears in the 1000–1130 cm^{-1} range, which is characteristic of the silica remaining in the nanotubes due to in-plane Si-O vibration bands. Typical halloysite peaks usually located at 3622 and 3695 cm^{-1} related to O–H stretching of Al–OH groups are effectively missing with the withdrawal of the inner layer [1,12] A FT-IR characterization was also performed on the nanotubes after the persulfate impregnation. The resulting spectra was identical to the one before the insertion, shown in Fig. 7, confirming that no persulfate was left adsorbed on the outer layer of the nanotubes.

XPS scan spectrum and deconvoluted C1s and N1s of the SiO$_2$-C$_3$N$_4$ composite and the g-C$_3$N$_4$ sample are displayed in Fig. 8. The composite sample (see Table 2) contains C, N, O and Si. The atomic Si/O ratio of 0.38 indicates that a 20% of the oxygen is in excess compared to the theoretical value. The C/N ratio is equal to 0.75, implies that none of the elements is in excess, although the PXRD and FT-IR results suggest the presence of melon in the structure which would be translated into a small amine surplus and, thus, in a smaller C/N ratio. C1s spectra shows mainly one carbon species, which corresponds to the C-N-C coordination and has a binding energy of 287.6 eV. A smaller peak, located at 284.5 eV is assigned to adventitious Carbon. In the g-C$_3$N$_4$ sample a small peak at 288.3 eV, related to C-O bonds appears. The N1s spectrum was separated into several binding energies. The main signal appears at 398.2 eV and corresponds to the C═N-C, the hybridized nitrogen in triazine rings [57], and it is followed by the tertiary nitrogen N–(C)$_3$ groups (399.2 eV) signal. There is a 0.3 eV displacement of the signal with respect to the same peak in the carbon nitride sample which could be due to an interaction with the nanotubes. Another small peak appears at 400.5 eV, which is assigned to the hydrogen-bound amines. These bind to the edges of the network in the form of C-NH$_2$ and 2 C-NH bonds [61] and its presence indicates the presence of melem-derivatives, being melon the most likely. The concentration of these bonds would decrease as the degree of condensation from the linear melon structure increases into a perfect g-C$_3$N$_4$ structure [53]. Thomas et al., [53]. O 1 s spectra of both samples is displayed in the bottom line. Sample with just C$_3$N$_4$ shows only one peak situated at 532.2 eV, assigned to O-C group, originating from adsorbed oxygen species [66]. Sample SiO$_2$-C$_3$N$_4$ displays two different peaks, the main peak, situated at 532.6 eV, is ascribed to SiO$_2$ bonds, while the secondary peak, at 533.8 eV and representing the 16% percent of oxygen can suggest that an interaction can have occurred between the nanotubes and the carbon nitride.

The optical properties of the samples were characterized by UV–vis absorption spectroscopy (see Fig. 9). The major absorption occurs below
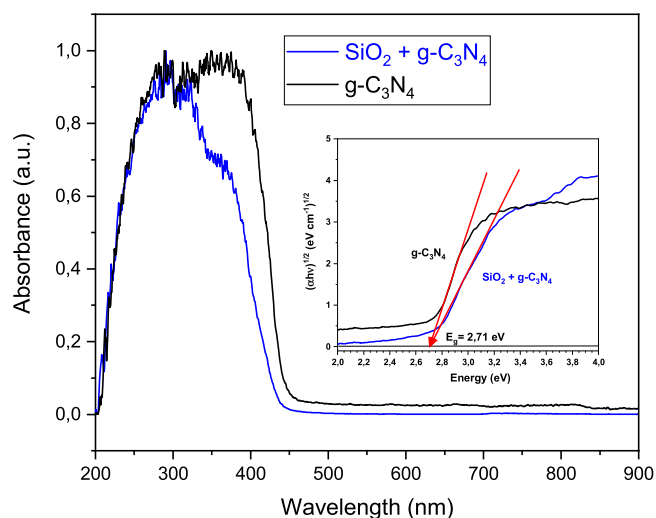
Table 2
Surface composition of SiO$_2$ nanotubes + g-C$_3$N$_4$ obtained by XPS.

Element	Name	Position	% Atomic concentration	% Atomic relation
C	C as graphite	284.5	4.5	30
	C–N–C	287.6	24.51	
	C 1 s, sat π-π	293.6	0.96	
O	Si-O	532.6	18.5	22
	O-?	533.8	3.51	
N	C═N-C	398.2	22.54	39.7
	N–(C)3	399.2	8.64	
	C–N–H	400.5	6.68	
	N 1 s, sat π-π	404, 406.2	1.79	
Si	Si 2p	103.2	8.36	8.4

450 nm and the slight hypsochromic shift that the composite sample experiences is related to its lighter color, as half the sample is composed of the white-colored nanotubes. However, this is not translated into their band gap adjustments as, based on the Tauc plots (inset Fig. 9), the band gap of the samples is similar at 2.71 eV. The effect of the nanotubes support on the migration, transfer and recombination of the photo-generated electron-hole pairs was studied by means of photo-luminescence (PL) [30]. The PL spectra of the two samples performed at an excitation wavelength of 365 nm are included in Fig. 10. The recombination of photoinduced electron-hole pairs is responsible for the PL emission in semiconductors and, thus, a lower PL intensity can be caused by a smaller recombination rate of the photogenerated electrons and holes, and a higher charge separation [30]. The higher dispersion of the carbon nitride together with the porous and unilayered structure of the nanotubes facilitates the separation of charge carriers which trans-lates into a quenched signal. An increase in photocatalytic activity could be expected as the existence of the photoinduced electron-hole pairs is lengthened [3].

3.2. Norfloxacin photodegradation performance

The effect of the nanotubes on the catalyst performance can be seen in Fig. 11. To begin with, the effect of the stirring process in dark mode marks a difference between the g-C$_3$N$_4$ sample and the composite with nanotubes. The adsorption effect of SiO$_2$ nanotubes causes a ∼ 45% reduction of the norfloxacin concentration. The experiments were per-formed with no pH modification (pH = 5). Norfloxacin has two pK$_a$ values (pK$_{a1}$ = 6.2 and pK$_{a2}$ = 8.5), which are related to the carboxyl group and the N4 atom in the piperazine moiety present in the com-pound, respectively [51]. At the pH of the experiment and up to 8.5 the cationic form as NH$_2^+$ is present. As the external surface of halloysite, the one remaining after the acid activation, is normally negatively charged [44], the adsorption capacity of the nanotubes gives an advantage in the form of the contaminant approach to the catalyst. In fact, experiments performed with no adsorption-desorption equilibrium phase show a reduction in the concentration of the antibiotic superior to 90% in less than 75 min (results no shown). SiO$_2$ nanotubes on their own, to detect if they were inert to photocatalytic activity [4] were also tested. Due to the composite absorbance result and its high BET surface) the amount chosen for the experiments was 10.8 mg instead of 20 mg (as is the amount of silica present in the SiO$_2$-C$_3$N$_4$ sample, 54% TGA results). Its adsorption capacity is indeed high (over 60% in the first 15 minutes but quickly stabilizes) and the photogeneration performance shows a little over 2% decrease in the amount has been recorded. The persulfate introduction in the nanotubes' lumens did not seem to modify their adsorption capacity. On the other hand, g-C$_3$N$_4$ had no adsorption ca-pacity and the concentration of Norfloxacin remained the same after 120 minutes. Once the visible lamp was switched-on, a rapid decrease in the drug concentration can be seen in all cases. The pseudo-first-kinetic constant (see Figure S2) of the g-C$_3$N$_4$ sample up to the minute 60 was

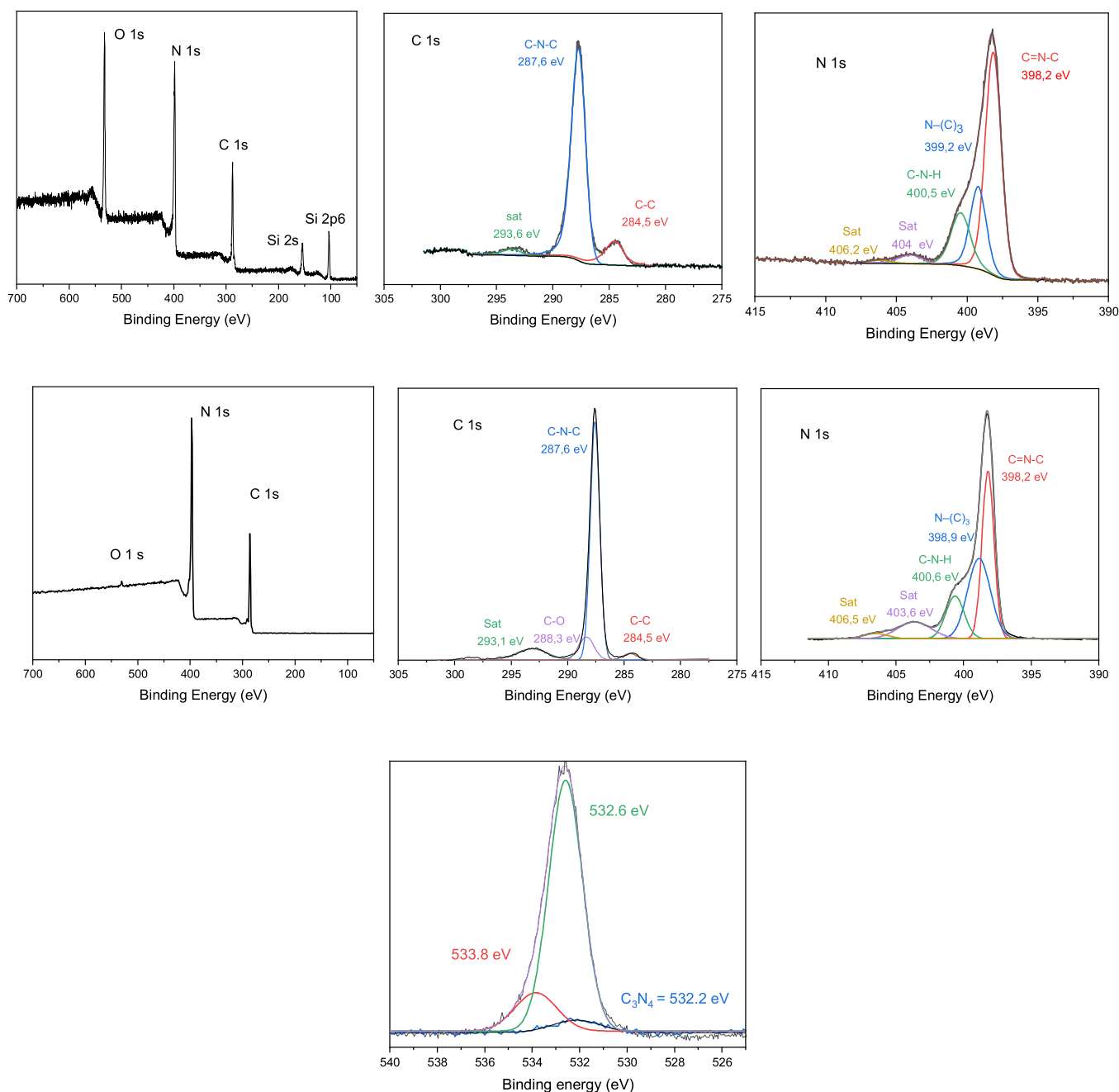**Fig. 8.** Diffuse reflectance UV–vis spectrum of the samples with their Tauc plot as an inset.

Fig. 9. XPS survey, C 1 s and N 1 s spectra of SiO_2-C_3N_4 sample (top line) and g-C_3N_4 sample (bottom line).

0.017 min^{-1}, whereas the use of SiO_2 nanotubes in the composite accelerated the degradation up to 0.023 min^{-1} (49% faster). The persulfate introduction in the system boosted the contaminant breakdown a further 47% with a 0.032 min^{-1} kinetic constant. These results agree with those reported by other authors for the photodegradation of Norfloxacin with the use of a g-C_3N_4 composite as catalyst (see Table 3). Photolysis test under visible light did not bring any reduction of the antibiotic concentration.

In order to try to decipher which active species participated in the degradation process, trapping experiments were conducted in ultrapure water with visible light and the SiO_2-C_3N_4 catalyst. Fig. 12 shows the effect of photogenerated holes (h$^+$), hydroxyl radicals (·OH) and superoxide radicals (·O$_2^-$) on the photodegradation of norfloxacin with the use of triethanolamine, tert-butanol and N$_2$ atmosphere, respectively. The photocatalytic performance of the composite was greatly inhibited after adding triethanolamine revealing that the photogenerated holes

were responsible, to a great extent, for the degradation of norfloxacin. In the same way, the presence of tert-butanol and the nitrogen atmosphere had only a slight effect on the photocatalysis process which could mean that, if any, they had only minima secondary roles in the process. The fact that the generation of hydroxyl radicals is not the main degradation pathway is coherent with the fact that the potential of both ·OH/OH$^-$ (2.38 eV, vs NHE) and ·OH /H$_2$O (2.72 eV, vs. NHE) potential is more positive than the valence band edge of g-C_3N_4 (1.65 eV, vs. NHE) although it could be formed indirectly [31]. The schematic diagram of the photoexcited electron-hole separation process for the persulfate-loaded g-C_3N_4-composite, from the collected experimental observations, is summarized in Fig. 13. The good activity shown by the three catalysts may be caused by the presence of heterojunctions within the melem/melem-derivatives/C_3N_4 lattice, as shown in PXRD and XPS characterization. The enhanced photocatalytic performance of the SiO_2-C_3N_4 catalyst could be attributed to the increment of surface area
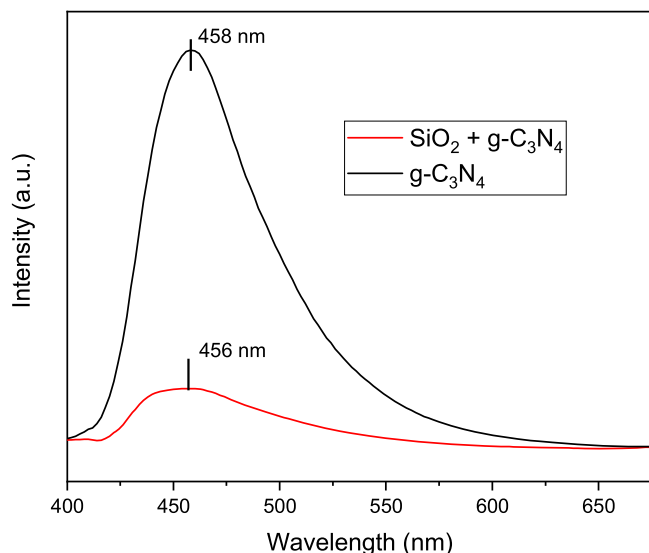
Fig. 10. Photoluminescent spectra of g-C$_3$N$_4$ and the SiO$_2$-C$_3$N$_4$ nanohybrid.

Fig. 12. Trapping experiments performed on SiO$_2$-C$_3$N$_4$ samples. Tert-butanol: scavengers for hydroxyl radicals (OH$^-$). Triethanolamine: scavenger for photo-generated holes (h$^+$). Inert N$_2$ atmosphere to quench superoxide radicals (·O$_2^-$).
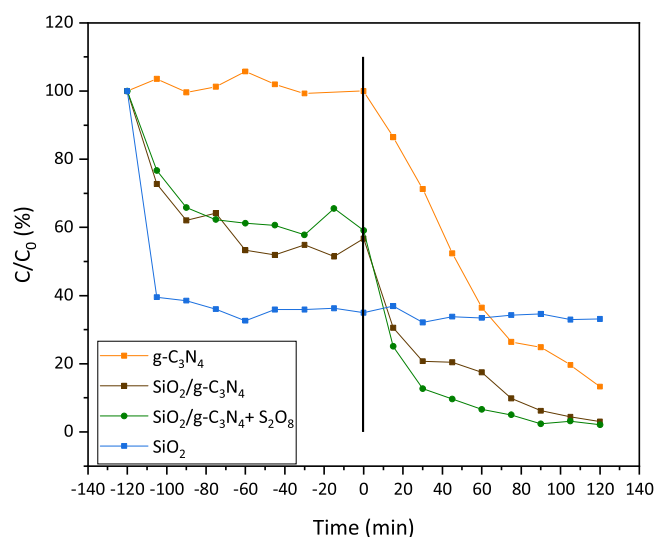
Fig. 11. Degradation behavior of g-C$_3$N$_4$, SiO$_2$-C$_3$N$_4$ and SiO$_2$-C$_3$N$_4$ with persulfate samples.

Fig. 13. Schematic diagram of the photoexcited electron-hole separation process for persulfate-loaded g-C$_3$N$_4$-composite.

4. Summary and conclusions

Silica nanotubes were tested as supports for the deposition of g-C$_3$N$_4$ in order to improve their photodegradation efficiency of the antibiotic Norfloxacin. Halloysite nanotubes were acid activated in order to strip them of the inner octahedral (Al-OH) layer but maintaining the outer tetrahedral (Si-O) one. This conferred the nanotubes a more than 300 m^2/g S$_{BET}$ increment and more than double the amount of g-C$_3$N$_4$ deposited on its surface. After the deposition the composite consisted of 46% g-C$_3$N$_4$. It granted the composite with adsorption capability and also its S$_{BET}$ was 5 times greater than the g-C$_3$N$_4$ sample used as a reference, which translated into a 49% increment in the degradation kinetics. The nanotube structure was exploited by loading persulfate into the lumens of the SiO$_2$-C$_3$N$_4$ which increased the degradation rate by 47%. The selected temperature for the polycondensation of melamine left some melem-derivatives in the structure forming heterojunctions which may be responsible for a great degradation performance of all the samples. The catalytic photoactivity of the composite studied with the use of scavengers revealed that the photogenerated holes were responsible to a great extent for the degradation of norfloxacin.

CRediT authorship contribution statement

leticia santamaria: Writing – original draft, Methodology,

Table 3
Pseudo-first-order kinetics of g-C$_3$N$_4$ composites in Norfloxacin degradation.

Sample	Pseudo-first-order kinetic (min^{-1})	Reference
ZnO/g-C$_3$N$_4$-Fe$_3$O$_4$	0.012	Chen et al., [8]
5%-CeO$_2$/g-C$_3$N$_4$	0.010	Liu et al., [37]
5%- CeO$_2$/g-C$_3$N$_4$ + persulfate	0.036	
NiWO$_4$@g-C$_3$N$_4$	0.055	S., Muthuraj
g-C$_3$N$_4$	0.015	[47]
15% N-doped ZnO/C$_3$N$_4$	0.034	Zhang et al., [68]
10% g-C$_3$N$_4$/Bi$_8$(CrO$_4$)O$_{11}$	0.038	Gu et al., [24]
g-C$_3$N$_4$	0.016	This work
g-C$_3$N$_4$/SiO$_2$ nanotubes	0.024	
g-C$_3$N$_4$/SiO$_2$ nanotubes + persulfate	0.032	

which could provide more surface reactive sites for improved charge separation and thus, visible light photocatalytic performance [27,52, 59].
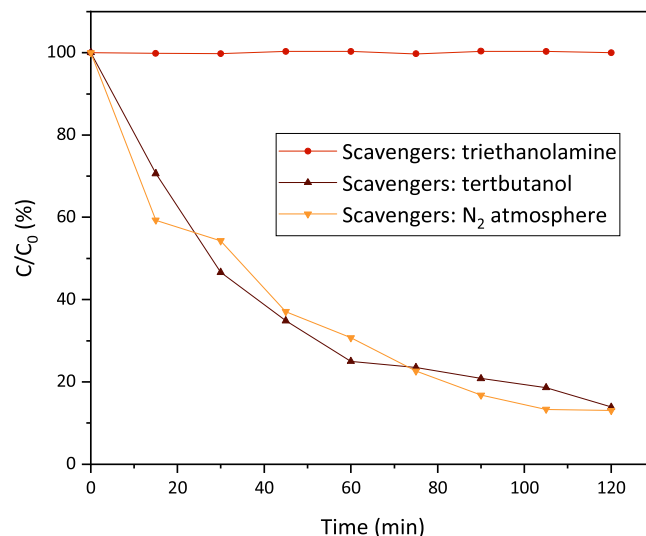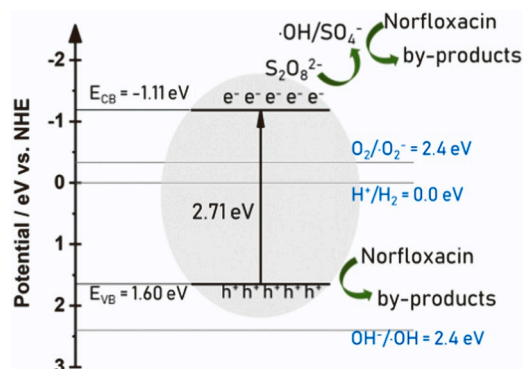
Appendix A. Supporting information

Supplementary data associated with this article can be found in the online version at doi:10.1016/j.cattod.2024.114584.

References

[1] G. Abdollahizad, F.M. Valadi, E. Akbarzadeh, M.R. Gholami, Adsorption properties of halloysite modified acrylamide/quince seeds-based hydrogel: experimental and DFT investigation, J. Polym. Environ. 30 (2022) 4637–4650, https://doi.org/10.1007/s10924-022-02537-8.

[2] M. Abid, A. Ben Haj Amara, M. Bechelany, Halloysite-TiO₂ Nanocomposites for water treatment: a review, Nanomaterials 13 (2023), https://doi.org/10.3390/nano13091578.

[3] E. Alwin, R. Wojcieszak, K. Kočí, M. Edelmannová, M. Zieliński, A. Suchora, T. Pędziński, M. Pietrowski, Reductive modification of carbon nitride structure by metals—the influence on structure and photocatalytic hydrogen evolution, Materials 15 (2022), https://doi.org/10.3390/ma15030710.

[4] C. Anastasescu, M. Zaharescu, D. Angelescu, C. Munteanu, V. Bratan, T. Spataru, C. Negrila, N. Spataru, I. Balint, Defect-related light absorption, photoluminiscence and photocatalytic activity of SiO₂ with tubular morphology, Sol. Energy Mater. Sol. Cells 159 (2017) 325–335, https://doi.org/10.1016/j.solmat.2016.09.032.

[5] M.J. Bojdys, J.O. Müller, M. Antonietti, A. Thomas, Ionothermal synthesis of crystalline, condensed, graphitic carbon nitride, Chem. A Eur. J. 14 (2008) 8177–8182, https://doi.org/10.1002/chem.200800190.

[6] A.J. Browne, M.G. Chipeta, G. Haines-Woodhouse, E.P.A. Kumaran, B.H. K. Hamadani, S. Zaraa, N.J. Henry, A. Deshpande, R.C. Reiner, N.P.J. Day, A. D. Lopez, S. Dunachie, C.E. Moore, A. Stergachis, S.I. Hay, C. Dolecek, Global antibiotic consumption and usage in humans, 2000–18: a spatial modelling study, Lancet Planet. Heal. 5 (2021) e893–e904, https://doi.org/10.1016/S2542-5196(21)00280-1.

[7] A. Cassini, L.D. Högberg, D. Plachouras, A. Quattrocchi, A. Hoxha, G.S. Simonsen, M. Colomb-Cotinat, M.E. Kretzschmar, B. Devleesschauwer, M. Cecchini, D. A. Ouakrim, T.C. Oliveira, M.J. Struelens, C. Suetens, D.L. Monnet, R. Strauss, K. Mertens, T. Struyf, B. Catry, K. Latour, I.N. Ivanov, E.G. Dobreva, A. Tambic Andrašević, S. Soprek, A. Budimir, N. Paphitou, H. Žemličková, S. Schytte Olsen, U. Wolff Sönksen, P. Märtin, M. Ivanova, O. Lyytikäinen, J. Jalava, B. Coignard, T. Eckmanns, M. Abu Sin, S. Haller, G.L. Daikos, A. Gikas, S. Tsiodras, F. Kontopidou, Á. Tóth, Á. Hajdu, Ó. Guólaugsson, K.G. Kristinsson, S. Murchan, K. Burns, P. Pezzotti, C. Gagliotti, U. Dumpis, A. Liuimiene, M. Perrin, M.A. Borg, S. C. de Greeff, J.C. Monen, M.B. Koek, P. Elstrøm, D. Zabicka, A. Deptula, W. Hryniewicz, M. Caniça, P.J. Nogueira, P.A. Fernandes, V. Manageiro, G. A. Popescu, R.I. Serban, E. Schréterová, S. Litvová, M. Štefkovicová, J. Kolman, I. Klavs, A. Korošec, B. Aracil, A. Asensio, M. Pérez-Vázquez, H. Billström, S. Larsson, J.S. Reilly, A. Johnson, S. Hopkins, Attributable deaths and disability-adjusted life-years caused by infections with antibiotic-resistant bacteria in the EU and the European Economic Area in 2015: a population-level modelling analysis, Lancet Infect. Dis. 19 (2019) 56–66, https://doi.org/10.1016/S1473-3099(18)30605-4.

[8] Q. Chen, Y. Hao, Z. Song, M. Liu, D. Chen, B. Zhu, J. Chen, Z. Chen, Optimization of photocatalytic degradation conditions and toxicity assessment of norfloxacin under visible light by new lamellar structure magnetic ZnO/g-C₃N₄, Ecotoxicol. Environ. Saf. 225 (2021) 112742, https://doi.org/10.1016/j.ecoenv.2021.112742.

[9] K.C. Christoforidis, M. Melchionna, T. Montini, D. Papoulis, E. Stathatos, S. Zafeiratos, E. Kordouli, P. Fornasiero, Solar and visible light photocatalytic enhancement of halloysite nanotubes/g-C₃N₄ heteroarchitectures, RSC Adv. 6 (2016) 86617–86626, https://doi.org/10.1039/c6ra15581b.

[10] I. Daou, G.L. Lecomte-Nana, N. Tessier-Doyen, C. Peyratout, M.F. Gonon, R. Guinebretiere, Probing the dehydroxylation of kaolinite and halloysite by in situ high temperature x-ray diffraction, Minerals 10 (2020), https://doi.org/10.3390/min10050480.

[11] R. Das, B.F. Leo, F. Murphy, The toxic truth about carbon nanotubes in water purification: a perspective view, Nanoscale Res. Lett. 13 (2018), https://doi.org/10.1186/s11671-018-2589-z.

[12] L. Deng, P. Yuan, D. Liu, P. Du, J. Zhou, Y. Wei, Y. Song, Y. Liu, Effects of calcination and acid treatment on improving benzene adsorption performance of halloysite, Appl. Clay Sci. 181 (2019) 105240, https://doi.org/10.1016/j.clay.2019.105240.

[13] X. Deng, F. Yao, Z. Wang, H. Zhao, B. Qi, Y. Zhou, H. Zhang, X. Zhou, Atom-dispersed Au combined with nano-Au on halloysite nanotubes with closo-dodecaborate promotes synergistic effects for enhanced photocatalysis, J. Mater. Chem. A 11 (2023) 809–817, https://doi.org/10.1039/D2TA07827A.

[14] H.V. Doan, H.T. Nguyen, V.P. Ting, S. Guan, J.C. Eloi, S.R. Hall, X.N. Pham, Improved photodegradation of anionic dyes using a complex graphitic carbon nitride and iron-based metal-organic framework material, Faraday Discuss. 231 (2021) 81–96, https://doi.org/10.1039/d1fd00010a.

[15] N. Eser, M. Önal, M. Çelik, A.D. Pekdemir, Y. Sarıkaya, Synthesis, characterization and some physicochemical properties of polypyrrole/halloysite composites, J. Macromol. Sci. Part A Pure Appl. Chem. 57 (2020) 222–228, https://doi.org/10.1080/10601325.2019.1691447.

[16] European Commission, 2022. Press release European Green Deal: Commission proposes rules for cleaner air and water. Ip/6278.

[17] European Environmental Agency, 2018. European waters. Assessment of status and pressures 2018, 7/2018.

[18] G.I. Fakhrullina, F.S. Akhatova, Y.M. Lvov, R.F. Fakhrullin, Toxicity of halloysite clay nanotubes in vivo: a caenorhabditis elegans study, Environ. Sci. Nano 2 (2015) 54–59, https://doi.org/10.1039/c4en00135d.

[19] X. Fan, Z. Xing, Z. Shu, L. Zhang, L. Wang, J. Shi, Improved photocatalytic activity of g-C₃N₄ derived from cyanamide-urea solution, RSC Adv. 5 (2015) 8323–8328, https://doi.org/10.1039/c4ra16362a.

[20] F. Fina, S.K. Callear, G.M. Carins, J.T.S. Irvine, Structural investigation of graphitic carbon nitride via XRD and neutron diffraction, Chem. Mater. 27 (2015) 2612–2618, https://doi.org/10.1021/acs.chemmater.5b00411.

[21] E. Fonseca, F. Hernández, A. Ibáñez, E. Pitarch, L. Bijlsma, Occurrence and ecological risks of pharmaceuticals in a Mediterranean river in Eastern Spain, Environ. Int. 144 (2020) 106004, https://doi.org/10.1016/j.envint.2020.106004.

[22] U.I. Gaya, A.H. Abdullah, Heterogeneous photocatalytic degradation of organic contaminants over titanium dioxide: a review of fundamentals, progress and problems, J. Photochem. Photobiol. C Photochem. Rev. 9 (2008) 1–12, https://doi.org/10.1016/j.jphotochemrev.2007.12.003.

[23] V. Geissen, H. Mol, E. Klumpp, G. Umlauf, M. Nadal, M. van der Ploeg, S.E.A.T. M. van de Zee, C.J. Ritsema, Emerging pollutants in the environment: a challenge for water resource management, Int. Soil Water Conserv. Res. 3 (2015) 57–65, https://doi.org/10.1016/j.iswcr.2015.03.002.

[24] X. Gu, T. Chen, J. Lei, Y. Yang, X. Zheng, S. Zhang, Q. Zhu, X. Fu, S. Meng, S. Chen, Self-assembly synthesis of S-scheme g-C₃N₄/Bi₈(CrO₄)O₁₁ for photocatalytic degradation of norfloxacin and bisphenol A, Chin. J. Catal. 43 (2022) 2569–2580, https://doi.org/10.1016/S1872-2067(22)64142-1.

[25] Q. Guo, Jingjing Zhao, Y. Yang, J. Huang, Y. Tang, X. Zhang, Z. Li, X. Yu, J. Shen, Junwei Zhao, Mesocrystalline Ta₃N₅ superstructures with long-lived charges for improved visible light photocatalytic hydrogen production, J. Colloid Interface Sci. 560 (2020) 359–368, https://doi.org/10.1016/j.jcis.2019.09.123.

[26] W. Guo, W. Liu, L. Xu, P. Feng, Y. Zhang, W. Yang, C. Shuai, Halloysite nanotubes loaded with nano silver for the sustained-release of antibacterial polymer nanocomposite scaffolds, J. Mater. Sci. Technol. 46 (2020) 237–247, https://doi.org/10.1016/j.jmst.2019.11.019.

[27] Y. Guo, C. Xin, L. Dai, Y. Zhang, X. Yu, Q. Guo, Layered and poriferous (Al,C)-Ta₂O₅ mesocrystals supported CdS quantum dots for high-efficiency photodegradation of organic contaminants, Sep. Purif. Technol. 284 (2022) 120297, https://doi.org/10.1016/j.seppur.2021.120297.

[28] V. Hasija, P. Raizada, V.K. Thakur, T. Ahmad, S.M. Alshehri, S. Thakur, V. H. Nguyen, Q. Van Le, P. Singh, An overview on photocatalytic sulfate radical formation via doped graphitic carbon nitride for water remediation, Curr. Opin. Chem. Eng. 37 (2022) 100841, https://doi.org/10.1016/j.coche.2022.100841.

[29] M. Hojamberdiev, M.M. Khan, Z. Kadirova, K. Kawashima, K. Yubuta, K. Teshima, R. Riedel, M. Hasegawa, Synergistic effect of g-C_3N_4, $Ni(OH)_2$ and halloysite in nanocomposite photocatalyst on efficient photocatalytic hydrogen generation, Renew. Energy 138 (2019) 434–444, https://doi.org/10.1016/j.renene.2019.01.103.

[30] J. Huang, S. Liu, W. Long, Q. Wang, X. Yu, S. Li, Highly enhanced photodegradation of emerging pollutants by $Ag/AgCl/Ta_2O_5−x$ mesocrystals, Sep. Purif. Technol. 279 (2021) 119733, https://doi.org/10.1016/j.seppur.2021.119733.

[31] M. Jiménez-Salcedo, M. Monge, M.T. Tena, The photocatalytic degradation of sodium diclofenac in different water matrices using g-C_3N_4 nanosheets: a study of the intermediate by-products and mechanism, J. Environ. Chem. Eng. 9 (2021) 0–8, https://doi.org/10.1016/j.jece.2021.105827.

[32] E. Joussein, S. Petit, J. Churchman, B. Theng, D. Righi, B. Delvaux, Halloysite clay minerals — a review, Clay Min. 40 (2005) 383–426, https://doi.org/10.1180/0009855054040180.

[33] S.R. Levis, P.B. Deasy, Characterisation of halloysite for use as a microtubular drug delivery system, Int. J. Pharm. 243 (2002) 125–134, https://doi.org/10.1016/S0378-5173(02)00274-0.

[34] S. Li, Y. Peng, C. Hu, Z. Chen, Self-assembled synthesis of benzene-ring-grafted g-C_3N_4 nanotubes for enhanced photocatalytic H_2 evolution, Appl. Catal. B Environ. 279 (2020) 119401, https://doi.org/10.1016/j.apcatb.2020.119401.

[35] S. Lin, S. Li, Y. Zhang, T. Ma, H. Huang, All-in-one polarized Co/CdS/halloysite ferroelectric hybrid for exceptional photocatalytic hydrogen evolution, J. Mater. Chem. A 9 (2021) 17936–17944, https://doi.org/10.1039/D1TA05247K.

[36] C. Liu, V. Nanaboina, G.V. Korshin, W. Jiang, Spectroscopic study of degradation products of ciprofloxacin, norfloxacin and lomefloxacin formed in ozonated wastewater, Water Res. 46 (2012) 5235–5246, https://doi.org/10.1016/j.watres.2012.07.005.

[37] W. Liu, J. Zhou, J. Yao, Shuttle-like CeO_2/g-C_3N_4 composite combined with persulfate for the enhanced photocatalytic degradation of norfloxacin under visible light, Ecotoxicol. Environ. Saf. 190 (2020) 110062, https://doi.org/10.1016/j.ecoenv.2019.110062.

[38] N. Lu, P. Wang, Y. Su, H. Yu, N. Liu, X. Quan, Construction of Z-Scheme g-C_3N_4/RGO/WO_3 with in situ photoreduced graphene oxide as electron mediator for efficient photocatalytic degradation of ciprofloxacin, Chemosphere 215 (2019) 444–453, https://doi.org/10.1016/j.chemosphere.2018.10.065.

[39] S. Mellouk, S. Cherifi, M. Sassi, K. Marouf-Khelifa, A. Bengueddach, J. Schott, A. Khelifa, Intercalation of halloysite from Djebel Debagh (Algeria) and adsorption of copper ions, Appl. Clay Sci. 44 (2009) 230–236, https://doi.org/10.1016/j.clay.2009.02.008.

[40] H.T. Nguyen, H.V. Doan, T.T.B. Nguyen, X.N. Pham, Nanoarchitectonics of Ag-modified g-C_3N_4@halloysite nanotubes by a green method for enhanced photocatalytic efficiency, Adv. Powder Technol. 33 (2022) 103862, https://doi.org/10.1016/j.apt.2022.103862.

[41] M. Nie, C. Zhou, W. Feng, C. Xin, X. Yu, Q. Li, Hierarchical ZnS layers-coated Ti^{3+}-TiO_2 nanostructures for boosted visible-light photocatalytic norfloxacin degradation, Colloids Surf. A Physicochem. Eng. Asp. 660 (2023) 130814, https://doi.org/10.1016/j.colsurfa.2022.130814.

[42] W.-J. Ong, L.-L. Tan, Y.H. Ng, S.-T. Yong, S.-P. Chai, Graphitic carbon nitride (g-C_3N_4)-based photocatalysts for artificial photosynthesis and environmental remediation: are we a step closer to achieving sustainability? Chem. Rev. 116 (2016) 7159–7329, https://doi.org/10.1021/acs.chemrev.6b00075.

[43] I. Papailias, T. Giannakopoulou, N. Todorova, D. Demotikali, T. Vaimakis, C. Trapalis, Effect of processing temperature on structure and photocatalytic properties of g-C_3N_4, Appl. Surf. Sci. 358 (2015) 278–286, https://doi.org/10.1016/j.apsusc.2015.08.097.

[44] D. Papoulis, Halloysite based nanocomposites and photocatalysis: a review, Appl. Clay Sci. 168 (2019) 164–174, https://doi.org/10.1016/j.clay.2018.11.009.

[45] K.M.M. Pärnänen, C. Narciso-Da-Rocha, D. Kneis, T.U. Berendonk, D. Cacace, T. T. Do, C. Elpers, D. Fatta-Kassinos, I. Henriques, T. Jaeger, A. Karkman, J. L. Martinez, S.G. Michael, I. Michael-Kordatou, K. O'Sullivan, S. Rodriguez-Mozaz, T. Schwartz, H. Sheng, H. Sørum, R.D. Stedtfeld, J.M. Tiedje, S.V.Della Giustina, F. Walsh, I. Vaz-Moreira, M. Virta, C.M. Manaia, Antibiotic resistance in European wastewater treatment plants mirrors the pattern of clinical antibiotic resistance prevalence, Sci. Adv. 5 (2019), https://doi.org/10.1126/sciadv.aau9124.

[46] X.N. Pham, H.T. Nguyen, T.N. Pham, T.T.B. Nguyen, M.B. Nguyen, V.T.T. Tran, H. V. Doan, Green synthesis of H-ZSM-5 zeolite-anchored O-doped g–C_3N_4 for photodegradation of Reactive Red 195 (RR 195) under solar light, J. Taiwan Inst. Chem. Eng. 114 (2020) 91–102, https://doi.org/10.1016/j.jtice.2020.09.018.

[47] L.P. S, V. Muthuraj, Superior visible light driven photocatalytic degradation of fluoroquinolone drug norfloxacin over novel $NiWO_4$ nanorods anchored on g-C_3N_4 nanosheets, Colloids Surf. A Physicochem. Eng. Asp. 567 (2019) 43–54, https://doi.org/10.1016/j.colsurfa.2019.01.040.

[48] W. Shen, D. Xiang, J. Yang, Y. Tang, C. Xin, Q. Guo, X. Yu, Fabrication of beta zeolite supported Ti^{3+}-TiO_2/CdS composite for ultrahigh-performance photodegradation of tetracycline under visible-light illumination, Colloids Surf. A Physicochem. Eng. Asp. 653 (2022) 129965, https://doi.org/10.1016/j.colsurfa.2022.129965.

[49] B. Song, Z. Zeng, G. Zeng, J. Gong, R. Xiao, S. Ye, M. Chen, C. Lai, P. Xu, X. Tang, Powerful combination of g-C_3N_4 and LDHs for enhanced photocatalytic performance: a review of strategy, synthesis, and applications, Adv. Colloid Interface Sci. 272 (2019) 1–17, https://doi.org/10.1016/j.cis.2019.101999.

[50] G.E. Stein, Review of the bioavailability and pharmacokinetics of oral norfloxacin, Am. J. Med. 82 (1987) 18–21, https://doi.org/10.1016/0002-9343(87)90613-9.

[51] M. Sui, Y. Zhou, L. Sheng, B. Duan, Adsorption of norfloxacin in aqueous solution by Mg-Al layered double hydroxides with variable metal composition and interlayer anions, Chem. Eng. J. 210 (2012) 451–460, https://doi.org/10.1016/j.cej.2012.09.026.

[52] Y. Tang, J. Huang, S. Liu, D. Xiang, X. Ma, X. Yu, M. Li, Q. Guo, Surface engineering induced superstructure $Ta_2O_5−x$ mesocrystals for enhanced visible light photocatalytic antibiotic degradation, J. Colloid Interface Sci. 596 (2021) 468–478, https://doi.org/10.1016/j.jcis.2021.03.118.

[53] A. Thomas, A. Fischer, F. Goettmann, M. Antonietti, J.O. Müller, R. Schlögl, J. M. Carlsson, Graphitic carbon nitride materials: variation of structure and morphology and their use as metal-free catalysts, J. Mater. Chem. 18 (2008) 4893–4908, https://doi.org/10.1039/b800274f.

[54] M. Thommes, K. Kaneko, A.V. Neimark, J.P. Olivier, F. Rodriguez-Reinoso, J. Rouquerol, K.S.W. Sing, Physisorption of gases, with special reference to the evaluation of surface area and pore size distribution (IUPAC Technical Report), Pure Appl. Chem. 87 (2015) 1051–1069, https://doi.org/10.1515/pac-2014-1117.

[55] H. Wang, J. Li, C. Ma, Q. Guan, Z. Lu, P. Huo, Y. Yan, Melamine modified P25 with heating method and enhanced the photocatalytic activity on degradation of ciprofloxacin, Appl. Surf. Sci. 329 (2015) 17–22, https://doi.org/10.1016/j.apsusc.2014.12.049.

[56] W. Wang, Z. Shu, J. Zhou, T. Li, P. Duan, Z. Zhao, Y. Tan, C. Xie, S. Cui, Halloysite-derived mesoporous g-C_3N_4 nanotubes for improved visible-light photocatalytic hydrogen evolution, Appl. Clay Sci. 158 (2018) 143–149, https://doi.org/10.1016/j.clay.2018.03.018.

[57] X. Wei, Y. Qiu, W. Duan, Z. Liu, Cathodic and anodic photocurrents generation from melem and its derivatives, RSC Adv. 5 (2015) 26675–26679, https://doi.org/10.1039/c5ra02816g.

[58] J. Wen, J. Xie, X. Chen, X. Li, A review on g-C_3N_4 -based photocatalysts, Appl. Surf. Sci. 391 (2017) 72–123, https://doi.org/10.1016/j.apsusc.2016.07.030.

[59] C. Xin, B. Wang, J. Yang, J. Zhao, X. Yu, Y. Tian, Construction of ZnS_{1-x} layers coated Nb_2O_{5-x} mesocrystals for boosted removal of organic contaminant, Ceram. Int. 49 (2023) 37861–37871, https://doi.org/10.1016/j.ceramint.2023.09.114.

[60] C. Xin, W. Wang, M. Xu, X. Yu, M. Li, S. Li, Construction of Au and C_{60} quantum dots modified materials of Institute Lavoisier-125(Ti) architectures for antibiotic degradation: performance, toxicity assessment, and mechanistic insight, J. Colloid Interface Sci. 623 (2022) 417–431, https://doi.org/10.1016/j.jcis.2022.05.028.

[61] S.C. Yan, Z.S. Li, Z.G. Zou, Photodegradation performance of g-C_3N_4 fabricated by directly heating melamine, Langmuir 25 (2009) 10397–10401, https://doi.org/10.1021/la900923z.

[62] Z. Yang, J. Yan, J. Lian, H. Xu, X. She, H. Li, g-C_3N_4/TiO_2 Nanocomposites for degradation of ciprofloxacin under visible light irradiation, ChemistrySelect 1 (2016) 5679–5685, https://doi.org/10.1002/slct.201600861.

[63] X. Yu, J. Huang, J. Zhao, C. Zhou, C. Xin, Q. Guo, Topotactic formation of poriferous (Al,C)–Ta_2O_5 mesocrystals for improved visible-light photocatalysis, J. Environ. Manag. 304 (2022) 114289, https://doi.org/10.1016/j.jenvman.2021.114289.

[64] X. Yu, Jingjing Zhao, J. Huang, Jiawei Zhao, Y. Guo, Y. Tang, X. Ma, Z. Li, Q. Guo, Junwei Zhao, Visible light photocatalysis of amorphous Cl-$Ta_2O_{5−x}$ microspheres for stabilized hydrogen generation, J. Colloid Interface Sci. 572 (2020) 141–150, https://doi.org/10.1016/j.jcis.2020.03.030.

[65] X. Yu, C. Zhou, Z. Huang, C. Xin, Y. Lin, F. Fu, S. Li, W. Zhang, Rational design of $AgCl@Zr^{3+}$-ZrO_2 nanostructures for ultra-efficient visible-light photodegradation of emerging pollutants, Appl. Catal. B Environ. 325 (2023) 122308, https://doi.org/10.1016/j.apcatb.2022.122308.

[66] Y. Zeng, C. Liu, L. Wang, S. Zhang, Y. Ding, Y. Xu, Y. Liu, S. Luo, A three-dimensional graphitic carbon nitride belt network for enhanced visible light photocatalytic hydrogen evolution, J. Mater. Chem. A 4 (2016) 19003–19010, https://doi.org/10.1039/C6TA07397B.

[67] A.B. Zhang, L. Pan, H.Y. Zhang, S.T. Liu, Y. Ye, M.S. Xia, X.G. Chen, Effects of acid treatment on the physico-chemical and pore characteristics of halloysite, Colloids Surf. A Physicochem. Eng. Asp. 396 (2012) 182–188, https://doi.org/10.1016/j.colsurfa.2011.12.067.

[68] C. Zhang, M. Jia, Z. Xu, W. Xiong, Z. Yang, J. Cao, H. Peng, H. Xu, Y. Xiang, Y. Jing, Constructing 2D/2D N-ZnO/g-C_3N_4 S-scheme heterojunction: efficient photocatalytic performance for norfloxacin degradation, Chem. Eng. J. 430 (2022) 132652, https://doi.org/10.1016/j.cej.2021.132652.

[69] X.L. Zhao, P. Li, S.Q. Zhang, S.W. He, S.Y. Xing, Z.H. Cao, R. Lu, Z.H. Li, Effects of environmental norfloxacin concentrations on the intestinal health and function of juvenile common carp and potential risk to humans, Environ. Pollut. 287 (2021) 117612, https://doi.org/10.1016/j.envpol.2021.117612.

[70] Y. Zhou, W. Lv, B. Zhu, F. Tong, J. Pan, J. Bai, Q. Zhou, H. Qin, Template-free one-step synthesis of g-C_3N_4 nanosheets with simultaneous porous network and S-doping for remarkable visible-light-driven hydrogen evolution, ACS Sustain. Chem. Eng. 7 (2019) 5801–5807, https://doi.org/10.1021/acssuschemeng.8b05374.